Draft version January 6, 2025
Typeset using LaTeX **twocolumn** style in AASTeX63

Observations of Microlensed Images with Dual-field Interferometry: On-sky Demonstration and Prospects

Przemek Mróz,[1] Subo Dong,[2, 3, 4] Antoine Mérand,[5] Jinyi Shangguan,[6] Julien Woillez,[5] Andrew Gould,[7, 8]
Andrzej Udalski,[1] Frank Eisenhauer,[6] Yoon-Hyun Ryu,[9] Zexuan Wu,[2, 3] Zhuokai Liu[2, 3] And Hongjing Yang[10]
—

Guillaume Bourdarot,[6] Denis Defrère,[11] Antonia Drescher,[6] Maximilian Fabricius,[6] Paulo Garcia,[12, 13]
Reinhard Genzel,[6] Stefan Gillessen,[6] Sebastian F. Hönig,[14] Laura Kreidberg,[8] Jean-Baptiste Le Bouquin,[15]
Dieter Lutz,[6] Florentin Millour,[16] Thomas Ott,[6] Thibaut Paumard,[17] Jonas Sauter,[6, 8] T. Taro Shimizu,[6]
Christian Straubmeier,[18] Matthias Subroweit[18] And Felix Widmann[6]

(The GRAVITY+ Collaboration)

Michał K. Szymański,[1] Igor Soszyński,[1] Paweł Pietrukowicz,[1] Szymon Kozłowski,[1] Radosław Poleski,[1]
Jan Skowron,[1] Krzysztof Ulaczyk,[19, 1] Mariusz Gromadzki,[1] Krzysztof Rybicki,[20, 1] Patryk Iwanek,[1]
Marcin Wrona[21, 1] And Mateusz J. Mróz[1]

(The OGLE Collaboration)

Michael D. Albrow,[22] Sun-Ju Chung,[9] Cheongho Han,[23] Kyu-Ha Hwang,[9] Youn Kil Jung,[9, 24] In-Gu Shin,[25]
Yossi Shvartzvald,[26] Jennifer C. Yee,[25] Weicheng Zang,[25] Sang-Mok Cha,[9, 27] Dong-Jin Kim,[9]
Seung-Lee Kim,[9] Chung-Uk Lee,[9] Dong-Joo Lee,[9] Yongseok Lee,[9, 27] Byeong-Gon Park[9]
And Richard W. Pogge[7, 28]

(The KMTNet Collaboration)

[1] *Astronomical Observatory, University of Warsaw, Al. Ujazdowskie 4, 00-478 Warszawa, Poland*
[2] *Department of Astronomy, School of Physics, Peking University, 5 Yiheyuan Road, Haidian District, Beijing 100871, People's Republic of China*
[3] *Kavli Institute of Astronomy and Astrophysics, Peking University, 5 Yiheyuan Road, Haidian District, Beijing 100871, People's Republic of China*
[4] *National Astronomical Observatories, Chinese Academy of Science, 20A Datun Road, Chaoyang District, Beijing 100101, People's Republic of China*
[5] *European Southern Observatory, Karl-Schwarzschild-Straße 2, D-85748 Garching, Germany*
[6] *Max Planck Institute for Extraterrestrial Physics, Giessenbachstraße 1, D-85748 Garching, Germany*
[7] *Department of Astronomy, Ohio State University, 140 West 18th Ave., Columbus, OH 43210, USA*
[8] *Max Planck Institute for Astronomy, Königstuhl 17, 69117 Heidelberg, Germany*
[9] *Korea Astronomy and Space Science Institute, Daejeon 34055, Republic of Korea*
[10] *Department of Astronomy, Tsinghua University, Beijing 100084, China*
[11] *Institute of Astronomy, KU Leuven, Celestijnenlaan 200D, 3001, Leuven, Belgium*
[12] *CENTRA – Centro de Astrofísica e Gravitação, IST, Universidade de Lisboa, 1049-001 Lisboa, Portugal*
[13] *Faculdade de Engenharia, Universidade do Porto, Rua Dr Roberto Frias, 4200-465 Porto, Portugal*
[14] *School of Physics & Astronomy, University of Southampton, Southampton, SO17 1BJ, UK*
[15] *Univ. Grenoble Alpes, CNRS, IPAG, 38000 Grenoble, France*
[16] *Université Côte d'Azur, Observatoire de la Côte d'Azur, CNRS, Laboratoire Lagrange, Nice, France*
[17] *LESIA, Observatoire de Paris, Université PSL, Sorbonne Université, Université Paris Cité, CNRS, 5 place Jules Janssen, 92195 Meudon, France*
[18] *1st Institute of Physics, University of Cologne, Zülpicher Straße 77, 50937 Cologne, Germany*
[19] *Department of Physics, University of Warwick, Coventry CV4 7 AL, UK*
[20] *Department of Particle Physics and Astrophysics, Weizmann Institute of Science, Rehovot 76100, Israel*
[21] *Department of Astrophysics and Planetary Sciences, Villanova University, 800 Lancaster Ave., Villanova, PA 19085, USA*
[22] *University of Canterbury, School of Physical and Chemical Sciences, Private Bag 4800, Christchurch 8020, New Zealand*

Corresponding author: Przemek Mróz
pmroz@astrouw.edu.pl

[23] *Department of Physics, Chungbuk National University, Cheongju 28644, Republic of Korea*
[24] *National University of Science and Technology (UST), Daejeon 34113, Republic of Korea*
[25] *Center for Astrophysics | Harvard & Smithsonian, 60 Garden St.,Cambridge, MA 02138, USA*
[26] *Department of Particle Physics and Astrophysics, Weizmann Institute of Science, Rehovot 7610001, Israel*
[27] *School of Space Research, Kyung Hee University, Yongin, Kyeonggi 17104, Republic of Korea*
[28] *Center for Cosmology and AstroParticle Physics, Ohio State University, 191 West Woodruff Ave., Columbus, OH 43210, USA*

(Received; Revised; Accepted)

ABSTRACT

Interferometric observations of gravitational microlensing events offer an opportunity for precise, efficient, and direct mass and distance measurements of lensing objects, especially those of isolated neutron stars and black holes. However, such observations have previously been possible for only a handful of extremely bright events. The recent development of a dual-field interferometer, GRAVITY Wide, has made it possible to reach out to significantly fainter objects and increase the pool of microlensing events amenable to interferometric observations by two orders of magnitude. Here, we present the first successful observation of a microlensing event with GRAVITY Wide and the resolution of microlensed images in the event OGLE-2023-BLG-0061/KMT-2023-BLG-0496. We measure the angular Einstein radius of the lens with subpercent precision, $\theta_{\rm E} = 1.280 \pm 0.009$ mas. Combined with the microlensing parallax detected from the event light curve, the mass and distance to the lens are found to be $0.472 \pm 0.012\,M_{\odot}$ and $1.81 \pm 0.05\,$kpc, respectively. We present the procedure for the selection of targets for interferometric observations and discuss possible systematic effects affecting GRAVITY Wide data. This detection demonstrates the capabilities of the new instrument, and it opens up completely new possibilities for the follow-up of microlensing events and future routine discoveries of isolated neutron stars and black holes.

Keywords: Gravitational microlensing (672), Optical interferometry (1168)

1. INTRODUCTION

In his seminal paper on gravitational microlensing, Einstein (1936) realized that the angular separation between the two images of the source star created by a Galactic gravitational lens would be well below the resolution limits of contemporary telescopes. That led him to believe that observing microlensed images would be, in practice, impossible. This notion persisted for many decades until the first optical interferometry facilities were developed.

In point-source point-lens microlensing events, the gravitational lens creates two images of the source star (called the major and minor image). They are separated by approximately $2\theta_{\rm E}$, where $\theta_{\rm E} = \sqrt{\kappa M \pi_{\rm rel}}$ is the angular Einstein radius. Here, M is the lens mass, $\pi_{\rm rel}$ is the lens–source relative parallax, and $\kappa = 8.144\,{\rm mas}\,M_{\odot}^{-1}$ is a constant. For typical configurations of stellar-mass microlensing events in the Milky Way, $\theta_{\rm E} \sim 1\,$mas, and so the expected separation between the minor and major images is usually smaller than a few milliarcseconds. Interferometric observations of microlensing events, therefore, provide a direct way to precisely measure angular Einstein radii by resolving the images (and, as a consequence, measure the masses of lensing objects).

Although a few tens of thousands of single-lens microlensing events have been discovered so far, only a few have had the angular Einstein radius measured. That was possible for only a small number of events exhibiting finite-source effects (Gould 1994; Nemiroff & Wickramasinghe 1994; Witt & Mao 1994), and the probability of such measurements is biased toward low-mass (planetary-mass) lenses. Another route for $\theta_{\rm E}$ measurements has involved astrometric observations (Hog et al. 1995; Miyamoto & Yoshii 1995; Walker 1995), leading to the first detection of an isolated black hole (Sahu et al. 2022; Lam et al. 2022; Mróz et al. 2022; Lam & Lu 2023). These observations, however, required long-term astrometric monitoring, which is not feasible for a large sample of events. Conversely, interferometric observations are much more efficient, as only one exposure is sufficient to resolve the microlensed images and measure the angular Einstein radius. When combined with the microlensing parallax ($\pi_{\rm E} \equiv \pi_{\rm rel}/\theta_{\rm E}$) measurements from the light curve, they allow us to precisely determine the masses, distances, and transverse velocities of isolated objects, including neutron stars and black holes.

Delplancke et al. (2001) were the first to discuss the prospects of using the European Southern Observatory (ESO) Very Large Telescope Interferometer (VLTI) to study gravitational microlensing events. They estimated that the first-generation VLTI instruments would be able to observe dozens of events every year in the mid 2000s. Yet, the first successful resolution of microlensed images did not materialize until late 2017, when Dong et al. (2019) observed the microlensing event TCP J05074264+2447555 (aka Kojima-1) with the second-generation VLTI instrument GRAVITY (GRAVITY Collaboration et al. 2017).

Why did it take almost two decades to achieve this milestone? The early predictions of VLTI performance underestimated the role and impact of many practical problems encountered during system operations, such as beam stability, vibrations, and air dispersion (e.g., Delplancke 2008). Moreover, even when these technical problems were solved or mitigated, the performance of a ground-based interferometer is ultimately limited by atmospheric turbulence, which breaks the coherence of the wave fronts arriving at each telescope. Therefore, the observations must be carried out with exposure times ($\sim 1\,\mathrm{ms}$) shorter than the typical wave-front-coherence timescale (on the order of 20–30 ms) and shorter than the mechanical vibrations timescale, which dominate in the 10–1000 Hz regime. Even for the largest modern 10 m class telescopes, this requirement sets a limiting magnitude of $K \approx 10$ for interferometric observations. Gravitational microlensing events brighter than this limit are exceedingly rare (Figure 1). They occur at most a few times a year, and they exceed the GRAVITY limiting magnitude for a short period of time. The three events with published interferometric observations were unusually bright: TCP J05074264+2447555 (Dong et al. 2019; Zang et al. 2020), ASASSN-22av (Wu et al. 2024a), and Gaia19bld (Cassan et al. 2022; Rybicki et al. 2022; Bachelet et al. 2022) reached $V \approx 11.5$, $g' \approx 12.5$, and $I \approx 9.0$, respectively. The former two were observed using the standard on-axis mode of GRAVITY, whose fringe tracker allows minute-long science exposures (Lacour et al. 2019) that significantly enhance the VLTI sensitivity (Eisenhauer et al. 2023).

The dual-field interferometric observations were designed to alleviate this problem and reach fainter sources (e.g., Shao & Colavita 1992; Colavita et al. 1999; Delplancke 2008; Woillez et al. 2014). In this observing mode, the target and a nearby bright ($K \lesssim 10$) reference (fringe-tracking) star are observed at the same time. The fringe-tracking star is needed to measure the atmospheric turbulence and stabilize the optical path difference between the telescopes, providing a correction to the science target. That enables observation of the target with exposure times longer than the turbulence and vibration timescales, allowing one to reach fainter objects. The angular separation between the science object and the fringe-tracking star must be smaller than $20'' - 30''$, which is set by the atmospheric conditions. In 2019–2022, the GRAVITY instrument was upgraded to enable such dual-field interferometric observations (GRAVITY+ Collaboration et al. 2022), hence the name of this observing mode, GRAVITY Wide.

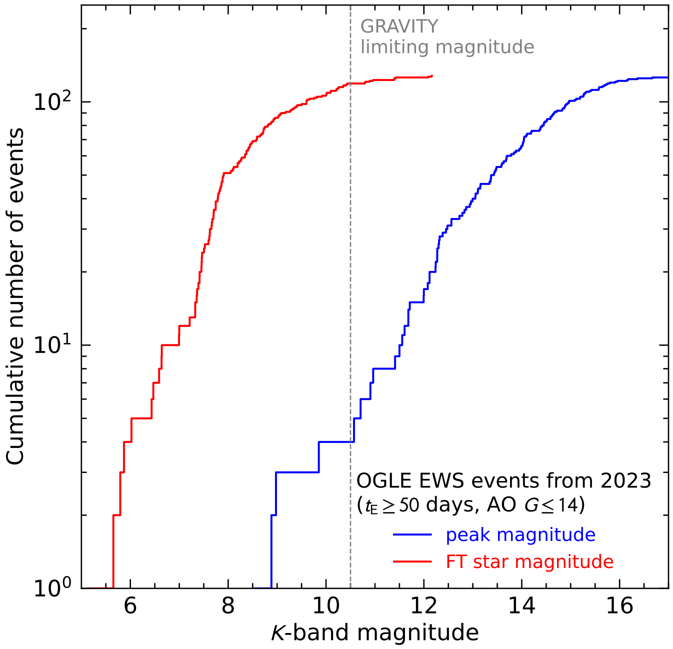

Figure 1. Cumulative distribution of the expected K-band peak magnitudes of events detected by the OGLE EWS in 2023 (blue line). For comparison, the red line shows the cumulative distribution of the K-band magnitudes of the brightest star within $30''$ of the event (fringe-tracking star). Only events with $t_{\mathrm{E}} \geq 50$ days and an adaptive optics guide star brighter than $G = 14$ are plotted.

The upgraded instrument opened up an entirely new pathway for characterizing and studying microlensing events because, in the dense fields of the Galactic bulge, the probability of finding a suitable ($K \lesssim 10$, within $30''$) fringe-tracking star is as large as 50%–70%. According to the GRAVITY manual (Issue 110),[1] the GRAVITY Wide observations are possible for science targets as faint as $K_{\mathrm{SC}} \approx$ 16–17. However, the limiting magnitude strongly depends on the atmospheric conditions and the separation between the science object and the fringe-tracking star. In addition, closure-phase observations lose the signal-to-noise ratio faster than normal visibility data as the targets become fainter. Thus, in practice, we rarely considered observing targets

---

[1] https://www.eso.org/sci/facilities/paranal/instruments/gravity.html

fainter than $K \approx 13.5$–14, which still left us with plenty of candidate events to scrutinize (Figure 1).

As soon as ESO offered regular GRAVITY Wide observations from October 2022 ("Period 110"), we initiated a program (PI: A. Mérand) of interferometric observations of microlensing events. Our primary science goal was to detect and measure precise masses, distances, and transverse velocities of isolated stellar remnants—neutron stars and black holes. Our observations also served as a test bed for verifying the capabilities of the new instrument and planning, executing, and analyzing interferometric follow-up observations of a large number of microlensing events.

This paper presents the first resolution of microlensed images with GRAVITY Wide in the microlensing event OGLE-2023-BLG-0061/KMT-2023-BLG-0496.

2. SELECTION OF THE TARGETS FOR INTERFEROMETRIC FOLLOW-UP

The VLTI observations can be carried out with either four 8.2 m Unit Telescopes (UTs) or four 1.8 m Auxiliary Telescopes (ATs). The VLTI UT observing runs are organized every month (around the full Moon) and typically last one week. During the rest of the month, observations are possible with ATs, which may be relocated to more than ten observing stations.[2] GRAVITY Wide observations may be conducted with ATs, provided that the fringe-tracking star is brighter than $K_{\mathrm{FT}} \approx 9$–9.5 and the science target is brighter than $K_{\mathrm{SC}} \approx 13$–14. For UTs, the limiting magnitudes are larger—$K_{\mathrm{FT}} \approx 10$–10.5 and $K_{\mathrm{SC}} \approx 16$–17, respectively. As discussed above, the limiting magnitudes of science targets strongly depend on the atmospheric conditions (isoplanatic angle) and the separation of the fringe-tracking star.

We began the selection of microlensing targets about 7–10 days before the planned start of each VLTI UT run. The candidates were chosen from publicly available lists of microlensing alerts published by the Optical Gravitational Lensing Experiment (OGLE) Early Warning System[3] (EWS; Udalski 2003; Udalski et al. 2015), the Korea Microlensing Telescope Network (KMTNet) Alert System[4] (Kim et al. 2018), and the Microlensing Observations in Astrophysics (MOA) Transient Alerts.[5] In addition, we also checked the transient alerts published by all-sky surveys, such as *Gaia* (Hodgkin et al. 2013, 2021) and the All Sky Automated Survey for SuperNovae (ASAS-SN; Shappee et al. 2014).

The selection of targets was based on several scientific and technical criteria. First, we selected events near or past their maximum brightness, so that the parameters describing their light curves were reasonably well measured. However, the observations had to be secured before the event faded, before the minor image became too faint, and so the contrast ratio between the microlensed images became too large. We required the contrast ratio to be smaller than 10:1, which was conservatively adopted based on our experience with the GRAVITY data. That contrast ratio corresponds to the maximum lens–source separation (in Einstein radius units) of $u_{\mathrm{max}} = 1.22$ or, equivalently, the minimum amplitude of $\Delta I_{\mathrm{min}} = 0.13$.

Because the primary scientific motivation of our project was searching for stellar remnants, which are expected to give rise to long-duration events, we selected events with Einstein timescales longer than $t_{\mathrm{E}} = 50$ days. However, the nature of the lens cannot be known at the time of selecting the targets. The mass of the lens can be determined only after the interferometric data are combined with the full light curve. That usually means waiting several weeks after the interferometric observations are taken, because they are collected close to the maximum magnification.

In the next step, we checked if suitable fringe-tracking and adaptive optics reference stars were located within $30''$ of the event. For possible fringe-tracking stars, we queried the Two Micron All Sky Survey (2MASS) Point Source Catalog (Skrutskie et al. 2006), while for adaptive optics guide stars, we queried *Gaia* Data Release 3 (Gaia Collaboration et al. 2016, 2023). The guide star had to be brighter than $G \approx 14$ for the Multi Application Curvature Adaptive Optics (Arsenault et al. 2003) system or brighter than $K = 8$ for the Coudé Infrared Adaptive Optics (Kendrew et al. 2012) system. Finally, we estimated the expected K-band brightness of the event during the planned observations, by assuming that the blending parameter in the K band was identical to that in the I band. The baseline K-band brightness of the event was taken from the VISTA Variables in the Via Lactea (VVV) survey (Minniti et al. 2010), the United Kingdom Infra-Red Telescope (UKIRT) Galactic Plane Survey (Lawrence et al. 2007; Lucas et al. 2008), or 2MASS (Skrutskie et al. 2006). We also examined the estimated K-band brightness of the source by using the best-fit I-band source fluxes as cross-checks. For such estimates, we assumed dereddened color $(I-K)_{0,\mathrm{giant}} = 1.4$ and $(I-K)_{0,\mathrm{dwarf}} = 1.0$ for sources roughly classi-

---

[2] https://www.eso.org/sci/facilities/paranal/telescopes/vlti.html

[3] https://ogle.astrouw.edu.pl/ogle4/ews/ews.html

[4] https://kmtnet.kasi.re.kr/~ulens/

[5] https://www.massey.ac.nz/~iabond/moa/alerts/

fied using the extinction-corrected source magnitudes as giants ($I_0 < 16.5$) and dwarfs ($I_0 > 16.5$), respectively.

Candidate targets were selected independently by two teams (P.M. and S.D.) and subsequently investigated in more detail. In particular, we paid special attention to the microlensing parallax measurements, which are necessary for the lens mass determination. Because the value of the microlensing parallax is inversely proportional to the square root of the lens mass, we required it to be consistent with zero (or close to zero) during the trigger. We also ran light-curve simulations to ensure that the parallax would be precisely measured (or constrained) by the end of the observing season. We did not consider events with variable source stars, because the variability may affect the microlensing parallax measurements.

The blue solid line in Figure 1 shows the cumulative distribution of the expected K-band peak magnitudes of the events detected by the OGLE EWS in 2023. Only events with relatively long timescales ($t_{\rm E} \geq 50\,$days) and suitable adaptive optics guide stars ($G \leq 14$) within $30''$ are presented. Only a few events were bright enough ($K < 10.5$) for standard GRAVITY on-axis observations. In contrast, the solid red line in Figure 1 shows the distribution of the K-band magnitudes of the brightest star within $30''$ of the event (which may serve as a fringe-tracking star). Nearly 100 events could have been considered for GRAVITY Wide observations.

3. DATA

The detection of the microlensing event OGLE-2023-BLG-0061 was announced by the OGLE EWS (Udalski 2003; Udalski et al. 2015) on 2023 March 13.60 UT ($\mathrm{HJD}' \equiv \mathrm{HJD} - 2460000 = 17.10$). It was independently identified by the KMTNet Alert System (Kim et al. 2016, 2018) on 2023 April 20, and it was designated KMT-2023-BLG-0496. The event occurred on a bright red clump star ($I = 16.389 \pm 0.001$, $V - I = 2.26 \pm 0.02$) with equatorial coordinates $(\mathrm{R.A.}, \mathrm{Decl.})_{\rm J2000} = (17^{\rm h}43^{\rm m}04\overset{\rm s}{.}01, -35^{\circ}15'32\overset{''}{.}3)$. According to data from the VVV survey, the source star had $K = 13.515 \pm 0.011$ (Minniti et al. 2010).

3.1. *Photometric Data*

OGLE operates the 1.3 m Warsaw Telescope located at Las Campanas Observatory, Chile. The telescope is equipped with a mosaic camera covering a field of view of $1.4\,\mathrm{deg}^2$ with a pixel scale of $0.26\,\mathrm{arcsec\,pixel}^{-1}$. The event has been observed by the OGLE-IV survey since 2010. However, in this paper, we analyze the OGLE data collected from 2016 through 2023, because earlier observations do not contribute to constraining the parameters of the model. Observations were reduced using the OGLE-IV data reduction pipeline (Udalski et al. 2015), which employs a custom implementation of the Difference Image Analysis (DIA) method (Woźniak 2000).

KMTNet uses three 1.6 m telescopes located at the Cerro Tololo Inter-American Observatory (KMTC; Chile), the South African Astronomical Observatory (KMTS; South Africa), and the Siding Spring Observatory (KMTA; Australia). Each of the KMTNet telescopes is equipped with a camera with a $4\,\mathrm{deg}^2$ field of view and a pixel scale of $0.40\,\mathrm{arcsec\,pixel}^{-1}$. The analyzed KMTNet observations cover the years 2021–2023. However, because of saturation, we deleted data points near the peak of the event. The KMTNet photometric data were reduced with the tender-loving-care (TLC) DIA-based pipeline (Yang et al. 2024), which was developed from pySIS (Albrow et al. 2009). The vast majority of OGLE and KMTNet images were taken in the I-band filter, with additional V-band observations to characterize the color of the source star.

Some additional observations were taken in the R' band with the 0.18 m Newtonian telescope (CHI-18; Wu et al. 2024b), located at the El Sauce Observatory in Chile, to cover the peak of the event. The CHI-18 images were reduced with the TLC pipeline. The original observations were taken at a 2 minutes cadence. Because the event did not exhibit variability on such short timescales, we binned the CHI-18 data into 1 hr long bins.

3.2. *VLTI Data*

OGLE-2023-BLG-0061/KMT-2023-BLG-0496 was considered a promising candidate for VLTI observations on 2023 July 20. Although the event was still before the peak, the available data predicted a relatively long timescale ($t_{\rm E} \approx 100$ days). At the same time, the optical brightness indicated that the microlens parallax should be robustly constrained. A nearby ($13.2''$) bright ($G = 13.7$, $K = 9.8$) star, 2MASS 17430426-3515195, could serve as a fringe-tracking and adaptive optics guide star. The first GRAVITY Wide observations were secured with UTs on 2023 July 29 ("epoch 1"). We obtained four sets of medium-resolution observations ($R = \lambda/\Delta\lambda \approx 500$) and one set of low-resolution data ($R \approx 22$), a new mode never tried before with GRAVITY Wide. The first three medium-resolution exposures were of low quality, and the resulting closure phases were very noisy. We therefore decided not to use them in the subsequent analysis. The preliminary modeling carried out at that time indicated that the

Table 1. Log of VLTI Observations

Epoch	Time	HJD$'$	Resolution	Exposure Time
1a	2023-07-29 02:59:45 UT	154.625	Medium	4 × 100 s
1b	2023-07-29 03:21:42 UT	154.640	Low	12 × 30 s
2a	2023-09-28 23:30:05 UT	216.479	Low	12 × 30 s
2b	2023-09-28 23:36:41 UT	216.484	Low	12 × 30 s
2c	2023-09-28 23:43:20 UT	216.488	Low	12 × 30 s
2d	2023-09-28 23:57:23 UT	216.498	Low	12 × 30 s
2e	2023-09-29 00:03:56 UT	216.503	Low	12 × 30 s
2f	2023-09-29 00:10:29 UT	216.507	Low	12 × 30 s

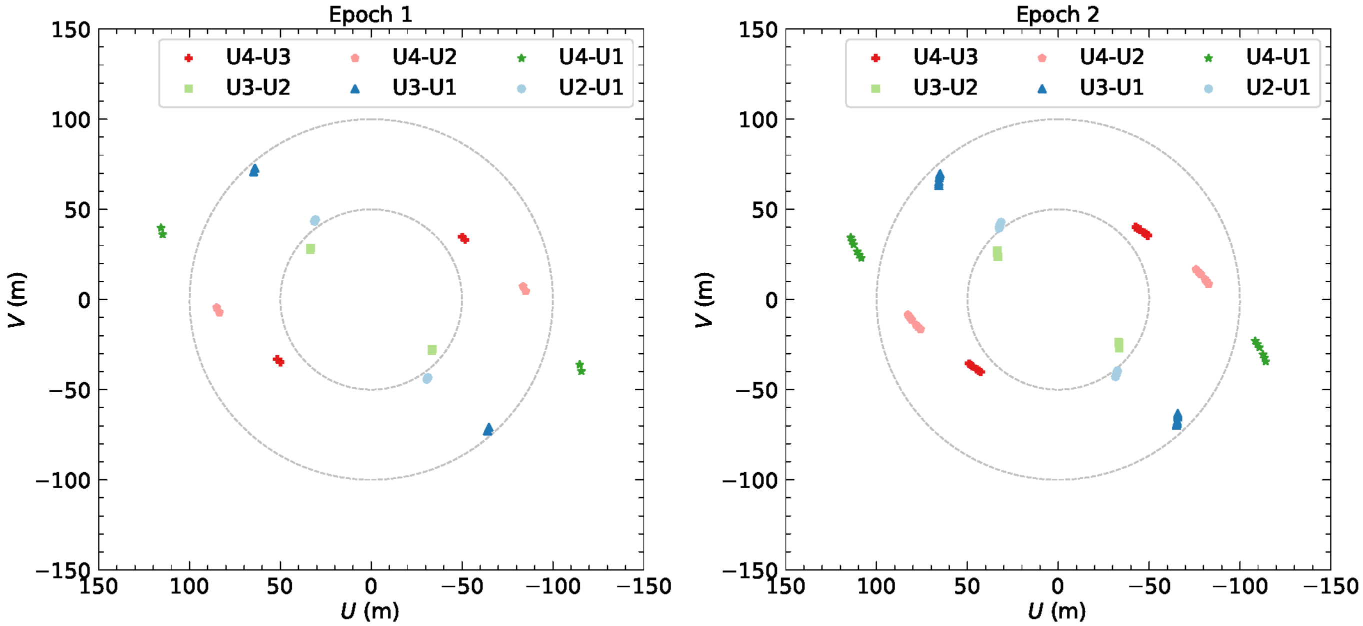

Figure 2. UV plane coverage of epoch 1 (left panel) and epoch 2 (right panel) GRAVITY observations of OGLE-2023-BLG-0061/KMT-2023-BLG-0496.

medium- and low-resolution data were inconsistent with each other.

We thus attempted to collect additional VLTI data to study the magnitude of the possible systematics affecting the low-resolution data. We triggered on-axis GRAVITY observations with ATs on 2023 August 23, when the event was approaching the peak (at magnification ∼ 90), but the data could not be collected. The next (successful) attempt to gather additional VLTI UT observations took place on 2023 September 29 ("epoch 2"), when we secured six low-resolution exposures with GRAVITY Wide. Table 1 presents the log of VLTI observations and Figure 2 shows the coverage of the UV plane during both VLTI epochs. Each low-resolution observation consisted of twelve 30 s exposures; the medium-resolution observation consisted of four 100 s exposures. For each night, a bright-star pair was observed to center the science fringe with the GRAVITY differential delay line before the microlens observation. We did not adjust the science fringe when the telescope was moved to the science target.

The data were reduced with the standard GRAVITY pipeline (version 1.4.2). We first used the Python script run_gravi_reduced.py to reduce the raw data and apply the pixel-to-visibility matrix (P2VM). The default options were used, except that we adopted –gravity_vis.output-phase-sc=SELF_VISPHI to calculate the internal differential phase between each spectral channel and –gravity_vis.opd-pupil-stddev-max-sc=9999 to ignore the poor pupil measurements in the acquisition camera, which do not affect our closure-phase measurements. The pipeline performed the bias and sky subtraction, flat-fielding, wavelength calibration, and spectral extraction. The application of the P2VM converts the pixel detector counts into complex visibilities, taking into account all instrumental effects, including relative throughput, coherence, phase shift, and crosstalk. The dark, bad-pixel, flat-field, wavelength calibration, and P2VM matrix data were reduced from the daily calibration data obtained close in time to our observations. We then used run_gravi_trend.py to calibrate the closure-phase data. For epoch 1, we used the star pair to center the science fringe and calibrate the medium-resolution data. Unfortunately, we did not have calibrator data observed in the low-resolution data on the same night. For epoch 2, we used a bright-star pair observed after the microlens observation for the calibration. The following analyses are based on the closure-phase data from the calibrated medium-resolution and uncalibrated low-resolution data from epoch 1 and the calibrated low-resolution data from epoch 2. In this way, we use all the data with good quality. Meanwhile, when modeling the low-resolution data from epoch 2, we found that the calibration makes little difference to the closure phase.

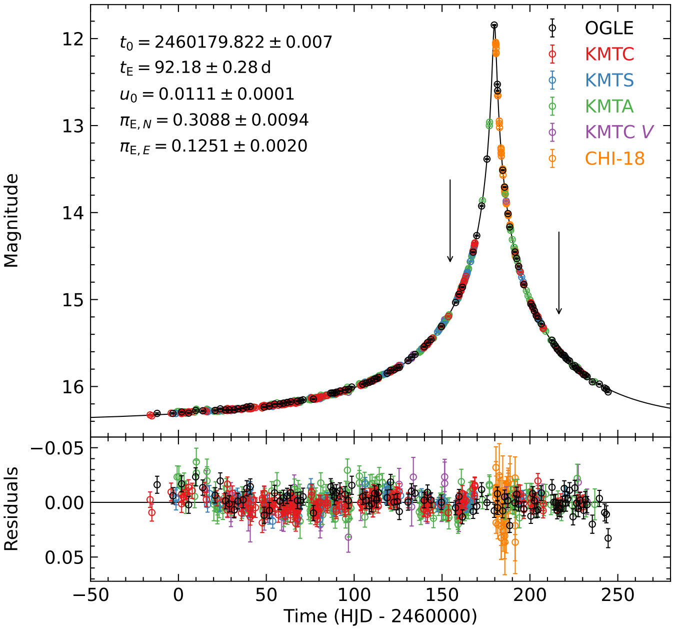

Figure 3. Light curve of OGLE-2023-BLG-0061/KMT-2023-BLG-0496. The black line marks the best-fit model with $u_0 > 0$. Arrows mark the two epochs of VLTI observations.

4. LIGHT-CURVE MODEL

The light curve of the event can be well fitted by a standard point-source point-lens model with the annual parallax effect (which is caused by the orbital motion of the Earth). This model has five free parameters: the time of closest approach between the lens and the source t_0, their minimum separation (in Einstein radius units) u_0, the Einstein radius crossing timescale t_E, and the northern and eastern components of the microlensing parallax vector $\boldsymbol{\pi}_E = (\pi_{E,N}, \pi_{E,E})$. The latter is a vector quantity whose direction is parallel to the direction of the relative lens–source proper motion $\boldsymbol{\mu}_{\rm rel}$. The magnification is calculated using the formula

$$A(t) = \frac{u(t)^2 + 2}{u(t)\sqrt{u(t)^2 + 4}}, \tag{1}$$

where $u(t) = \sqrt{\tau(t)^2 + \beta(t)^2}$. The latter quantity is evaluated in the geocentric frame that is moving with a velocity equal to the Earth's velocity at $t_{0,\rm par} = 2460179$ (Gould 2004) in which

$$\tau(t) = \frac{t - t_0}{t_E} + \delta\tau(t), \quad \beta(t) = u_0 + \delta\beta(t) \tag{2}$$

and

$$(\delta\tau, \delta\beta) = (\boldsymbol{\pi}_E \cdot \Delta s, \boldsymbol{\pi}_E \times \Delta s), \tag{3}$$

where Δs is the projected position of the Sun. Two models with different signs of u_0 are possible; both models are almost perfectly degenerate, with the $u_0 < 0$ model being preferred by only $\Delta\chi^2 = 3.1$. The best-fit model (with $u_0 > 0$) is presented in Figure 3. The best-fit parameters and their uncertainties are reported in Table 2. In Table 2, we also report the best-fit source magnitude I_s, baseline magnitude I_0, and dimensionless blending parameter f_s.

Figure 4 shows the constraints on the microlensing parallax vector derived using data from different observatories. The blue, red, green, and orange contours mark the constraints from OGLE, KMTC, KMTA, and KMTS data, respectively, whereas the solid black contours mark the best-fit model to all data. The eastern component of $\boldsymbol{\pi}_E$, which is parallel to the projected acceleration of the Sun, is relatively well measured in all data sets. However, the northern component $\pi_{E,N}$ (perpendicular to the projected acceleration of the Sun) has a considerably larger uncertainty. The northern component is also more susceptible to noise in the data (Gould et al. 1994; Smith et al. 2003; Gould 2004); hence, slightly different values of $\pi_{E,N}$ are determined using different data sets. The best-fit parameters for individual data sets are reported in Tables 3 and 4.

The light-curve model of a microlensing event makes it possible to predict the brightness ratio η between the minor and major image at a given epoch of interferometric

Table 2. Best-fit Parameters of the Light-curve Model

Parameter	$u_0 > 0$	$u_0 < 0$
t_0 (HJD$'$)	179.8223 ± 0.0066	179.8103 ± 0.0063
u_0	0.01112 ± 0.00008	-0.01112 ± 0.00008
$t_{\rm E}$ (days)	92.18 ± 0.28	91.93 ± 0.28
$\pi_{{\rm E},N}$	0.3088 ± 0.0094	0.3222 ± 0.0099
$\pi_{{\rm E},E}$	0.1251 ± 0.0020	0.1245 ± 0.0021
χ^2/dof	$2093.7/2069$	$2090.6/2069$
$\pi_{\rm E}$	0.3330 ± 0.0084	0.3454 ± 0.0090
Φ_π (deg)	22.07 ± 0.81	21.13 ± 0.81
$f_{\rm s}$ (OGLE)	0.7392 ± 0.0030	0.7353 ± 0.0029
$I_{\rm s}$ (OGLE)	16.717 ± 0.005	16.723 ± 0.005
I_0 (OGLE)	16.389 ± 0.001	16.389 ± 0.001
$u(1)$	0.2640 ± 0.0008	0.2629 ± 0.0008
$\eta(1)$	0.5907 ± 0.0009	0.5920 ± 0.0009
$\phi(1)$ (deg)	173.11 ± 0.15	177.73 ± 0.15
PA(1) (deg)	-164.83 ± 0.95	-156.60 ± 0.68
$u(2)$	0.4295 ± 0.0015	0.4279 ± 0.0015
$\eta(2)$	0.4264 ± 0.0013	0.4277 ± 0.0013
$\phi(2)$ (deg)	9.46 ± 0.24	6.84 ± 0.26
PA(2) (deg)	31.52 ± 0.58	14.29 ± 1.06

Note—Parameters denoted by (1) and (2) were calculated for the VLTI epochs 1 and 2, respectively.

observations. Moreover, the detection of the microlensing parallax in the light curve allows us to predict the orientation of microlensed images in the sky. The position angle (PA; north through east) of the microlensing parallax vector can be calculated using the formula

$$\Phi_\pi = \arctan \frac{\pi_{{\rm E},E}}{\pi_{{\rm E},N}}. \tag{4}$$

The angle ϕ between the source–lens relative proper motion and source–lens relative position at a given time can also be calculated directly from the parameters of the light-curve model:

$$\phi(t) = \arctan \frac{\beta(t)}{\tau(t)}. \tag{5}$$

Note that in the limit of no parallax, this equation simplifies to $\phi(t) = \arctan(u_0 t_{\rm E}/(t - t_0))$, which is equivalent to Equation (8) derived by Dong et al. (2019). Then, following Dong et al. (2019), the position angle of the minor image relative to the major image (north through east) is simply PA $= \Phi_\pi + \phi$ if $u_0 > 0$ or PA $= \Phi_\pi - \phi$ if $u_0 < 0$. These two cases depend on the trajectory of the lens relative to the source: $u_0 > 0$ if the lens passes the source on its right and $u_0 < 0$ on its left (Skowron et al. 2011). Note that Dong et al. (2019) introduced a different definition of the position angle of the major image relative to the minor image: $\psi = {\rm PA} + \pi$.

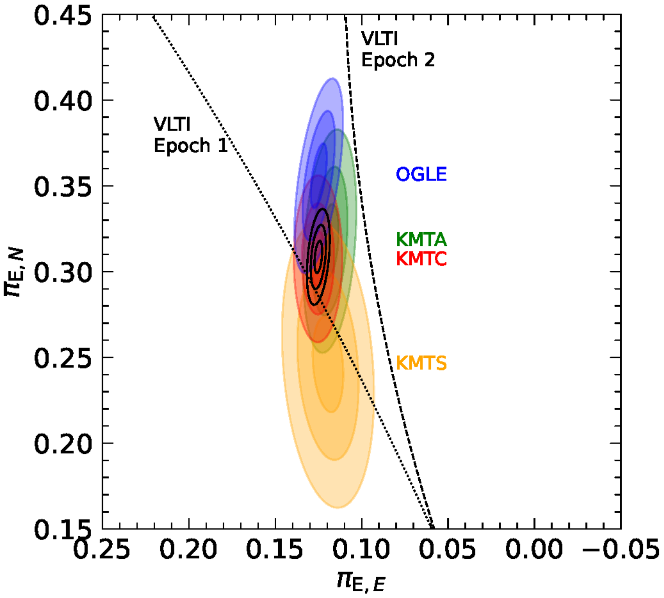

Figure 4. Constraints on the microlensing parallax derived from different photometric data sets (blue—OGLE; red—KMTC; orange—KMTS; and green—KMTA) and all light-curve data (black contours). The dotted and dashed lines mark the constraints from the two epochs of VLTI data, respectively.

Table 2 presents the predicted lens–source separation u (in Einstein radius units), the flux ratio between the minor and major image η, and the position angle of the images PA for both epochs of VLTI observations. Note that the expected lens–source separation and flux ratio of the images are virtually identical for the $u_0 > 0$ and $u_0 < 0$ models. However, the expected position angles are different. For the positive u_0 solution, we can predict PA $= -164.83 \pm 0.95$ deg and PA $= 31.52 \pm 0.58$ deg for both VLTI epochs. For the negative u_0 solution, we predict PA $= -156.60 \pm 0.68$ deg and PA $= 14.29 \pm 1.06$ deg, respectively.

We also note that the flux ratio of the images is tightly constrained by the light-curve model, with a precision better than 0.3%. Conversely, the uncertainty of the position angle is dominated by the uncertainty in the determination of the angle Φ_π, which itself is dominated by the uncertainty of $\pi_{{\rm E},N}$. As we observed small systematic differences between $\pi_{{\rm E},N}$ determined using different data sets (Figure 4), these differences propagate to systematic variations in Φ_π and therefore PA. In particular, the angle Φ_π can vary from 18.56 to 25.90 deg (Tables 3 and 4).

Table 3. Best-fit Parameters of the Light-curve Model ($u_0 > 0$) for Individual Data Sets

Parameter	OGLE	KMTC	KMTS	KMTA
t_0 (HJD')	179.8290 ± 0.0082	179.8135 ± 0.0313	179.8279 ± 0.0401	179.8406 ± 0.0189
u_0	0.01099 ± 0.00011	0.00745 ± 0.00432	0.00841 ± 0.00472	0.00806 ± 0.00112
$t_{\rm E}$ (days)	93.57 ± 0.53	91.32 ± 0.70	93.89 ± 1.43	93.97 ± 0.74
$\pi_{{\rm E},N}$	0.3559 ± 0.0199	0.3076 ± 0.0162	0.2463 ± 0.0282	0.3182 ± 0.0220
$\pi_{{\rm E},E}$	0.1248 ± 0.0039	0.1252 ± 0.0047	0.1194 ± 0.0088	0.1184 ± 0.0050
χ^2/dof	542.9/541	600.8/632	329.3/329	417.2/417
$\pi_{\rm E}$	0.3772 ± 0.0178	0.3321 ± 0.0150	0.2738 ± 0.0263	0.3395 ± 0.0200
Φ_π (deg)	19.33 ± 1.52	22.15 ± 1.37	25.90 ± 2.93	20.41 ± 1.78
$u(1)$	0.2601 ± 0.0014	0.2661 ± 0.0022	0.2593 ± 0.0041	0.2592 ± 0.0019
$\eta(1)$	0.5953 ± 0.0016	0.5882 ± 0.0026	0.5962 ± 0.0048	0.5964 ± 0.0023
$\phi(1)$ (deg)	172.30 ± 0.32	173.98 ± 0.96	174.56 ± 1.15	173.50 ± 0.45
PA(1) (deg)	-168.37 ± 1.83	-163.90 ± 1.75	-159.58 ± 3.50	-166.08 ± 2.17
$u(2)$	0.4254 ± 0.0025	0.4328 ± 0.0039	0.4354 ± 0.0066	0.4204 ± 0.0039
$\eta(2)$	0.4298 ± 0.0021	0.4275 ± 0.0037	0.4149 ± 0.0073	0.4340 ± 0.0033
$\phi(2)$ (deg)	10.79 ± 0.54	8.87 ± 0.69	7.65 ± 0.97	9.50 ± 0.62
PA(2) (deg)	30.12 ± 0.99	31.08 ± 1.11	33.62 ± 2.30	29.91 ± 1.23

Table 4. Best-fit Parameters of the Light-curve Model ($u_0 < 0$) for Individual Data Sets

Parameter	OGLE	KMTC	KMTS	KMTA
t_0 (HJD')	179.8150 ± 0.0082	179.8063 ± 0.0304	179.8206 ± 0.0393	179.8324 ± 0.0193
u_0	-0.01098 ± 0.00010	-0.00798 ± 0.00434	-0.00851 ± 0.00461	-0.00799 ± 0.00113
$t_{\rm E}$ (days)	93.29 ± 0.53	91.10 ± 0.73	93.68 ± 1.45	93.75 ± 0.78
$\pi_{{\rm E},N}$	0.3699 ± 0.0198	0.3172 ± 0.0176	0.2557 ± 0.0299	0.3281 ± 0.0219
$\pi_{{\rm E},E}$	0.1243 ± 0.0039	0.1252 ± 0.0046	0.1190 ± 0.0088	0.1183 ± 0.0050
χ^2/dof	541.9/541	600.7/632	329.3/329	416.9/417
$\pi_{\rm E}$	0.3902 ± 0.0178	0.3410 ± 0.0165	0.2822 ± 0.0277	0.3489 ± 0.0201
Φ_π (deg)	18.56 ± 1.43	21.55 ± 1.32	24.98 ± 2.93	19.84 ± 1.71
$u(1)$	0.2587 ± 0.0014	0.2655 ± 0.0021	0.2588 ± 0.0039	0.2584 ± 0.0020
$\eta(1)$	0.5969 ± 0.0017	0.5890 ± 0.0024	0.5969 ± 0.0045	0.5973 ± 0.0024
$\phi(1)$ (deg)	176.93 ± 0.32	177.18 ± 0.89	178.12 ± 0.93	176.89 ± 0.38
PA(1) (deg)	-158.36 ± 1.12	-155.60 ± 1.55	-153.11 ± 2.85	-157.05 ± 1.47
$u(2)$	0.4235 ± 0.0025	0.4319 ± 0.0038	0.4178 ± 0.0076	0.4194 ± 0.0040
$\eta(2)$	0.4314 ± 0.0021	0.4243 ± 0.0032	0.4362 ± 0.0064	0.4349 ± 0.0034
$\phi(2)$ (deg)	8.20 ± 0.54	7.03 ± 0.57	5.54 ± 0.80	7.58 ± 0.57
PA(2) (deg)	10.36 ± 1.96	14.51 ± 1.65	19.44 ± 3.48	12.25 ± 2.24

5. CLOSURE-PHASE MODELS

The VLTI/GRAVITY observations of OGLE-2023-BLG-0061/KMT-2023-BLG-0496 provide a complementary view of the microlensing event. In particular, the spatial resolution of the interferometer allows us to resolve the microlensed images, providing a precise measurement of the angular Einstein radius. This information is not included in the light curve of the event. We first separately analyze the VLTI data collected during epochs 1a, 1b, and 2, because they were taken at different times and using different instrument configurations. That will allow us to study the consistency between the model parameters derived using different data sets and the consistency with the light-curve model (Sections 5.1, 5.2, and 5.3). In Section 5.4, we combine all VLTI data sets to derive the final parameters of the system. The results presented in this section were independently checked using the PMOIRED software[6] (Mérand 2022) and we found virtually identical results.

5.1. *No-lens-light Model*

In the simplest case, if the lens is dark and there are no other blended stars in the GRAVITY field of view, the two images of the source created by microlensing look like a mundane "binary star." We start by fitting such a simple binary star model to the closure-phase data. We assume that both images of the source star can be considered as point-like. We place the major image in the origin of the coordinate system, whereas the position of the minor image is parameterized by a vector $(\Delta\alpha, \Delta\delta)$. If we denote the flux ratio between the minor and major image as η, then the complex visibility is

$$\hat{V} = \frac{1 + \eta \exp\left(-\frac{2\pi i}{\lambda}\left(U\Delta\alpha + V\Delta\delta\right)\right)}{1+\eta}, \qquad (6)$$

where λ is the wavelength of observations and (U, V) is the separation of the telescopes in the UV plane. The visibility can be calculated for all possible pairs of telescopes ($\hat{V}_{1,2}$,$\hat{V}_{1,3}$,$\hat{V}_{1,4}$,..., where the indices denote different telescopes). For a triangle of telescopes, one can define the bispectrum as the product $B_{1,2,3} = \hat{V}_{1,2}\hat{V}_{2,3}\hat{V}_{3,1}$, and then the closure phase (denoted hereafter as T3) is the argument of this bispectrum $\mathrm{T3}_{1,2,3} = \arg\left(B_{1,2,3}\right)$ (see, Dalal & Lane 2003). Closure phases can be calculated for all possible triangles formed by the telescopes of the interferometer. For VLTI, there are four possible closure phases. In theory, one of them is not independent. However, because the measured closure phases may be affected by noise in the data, we employ all four closure-phase sets in the fits.

Table 5. Best-fit Parameters of the Closure-phase Model Without the Lens Light

Parameter	Epoch 1a	Epoch 1b	Epoch 2
$\Delta\alpha$ (mas)	-0.760 ± 0.012	-0.652 ± 0.030	1.163 ± 0.007
$\Delta\delta$ (mas)	-2.467 ± 0.018	-2.545 ± 0.029	2.309 ± 0.022
η	0.6168 ± 0.0096	0.6358 ± 0.0127	0.4414 ± 0.0098
σ_0 (deg)	7.04 ± 0.33	$2.76^{+0.46}_{-0.40}$	2.56 ± 0.26
s (mas)	2.581 ± 0.015	2.627 ± 0.022	2.585 ± 0.020
PA (deg)	-162.87 ± 0.36	-165.63 ± 0.77	26.74 ± 0.27
u	0.2424 ± 0.0075	0.2266 ± 0.0107	0.4120 ± 0.0119
θ_{E} (mas)	1.2814 ± 0.0066	1.3050 ± 0.0107	1.2660 ± 0.0083
χ^2/dof	824.5/924	49.6/48	282.6/308

We first conduct the grid search to find the initial parameters of the model. We keep the flux ratio fixed to $\eta = 0.591$ (epoch 1) and $\eta = 0.426$ (epoch 2)—that is, the best-fit values from the light-curve model (Table 2). We then evaluate the goodness-of-the-fit statistic χ^2 on a grid of 201×201 points uniformly distributed over the range $-10\,\mathrm{mas} \leq (\Delta\alpha, \Delta\delta) \leq 10\,\mathrm{mas}$. For each case, we find there is only one significant minimum of the χ^2 surface.

We then refine the results of the grid search by allowing all parameters to vary. This is achieved by maximizing the log-likelihood function defined as

$$\begin{aligned} \ln\mathcal{L} = &-\frac{1}{2}\sum_{i=1}^{4n_{\mathrm{exp}}}\sum_{j=1}^{\Lambda}\frac{(\mathrm{T3}_{ij} - \mathrm{T3}_{ij}^{\mathrm{model}})^2}{\sigma(\mathrm{T3})_{ij}^2 + \sigma_0^2} + \\ &-\frac{1}{2}\sum_{i=1}^{4n_{\mathrm{exp}}}\sum_{j=1}^{\Lambda}\ln\left(\sigma(\mathrm{T3})_{ij}^2 + \sigma_0^2\right), \end{aligned} \qquad (7)$$

where n_{exp} is the number of exposures in the epoch and Λ is the number of spectral channels. Because the error bars calculated from the pipeline may be underestimated, we add a constant error term σ_0 in quadrature. The best-fit parameters and their uncertainties are calculated using the Markov Chain Monte Carlo (MCMC) algorithm coded by Foreman-Mackey et al. (2013). We assume flat (noninformative) priors on all parameters of the model.

The results of the fits—separately for VLTI epochs 1a, 1b, and 2—are reported in Table 5. The best-fitting closure-phase models are shown in Figures 5 and 6. In addition to four model parameters, we report four derived quantities: the separation between the images $s = \sqrt{\Delta\alpha^2 + \Delta\delta^2}$, their position angle (north through

---

[6] https://github.com/amerand/PMOIRED

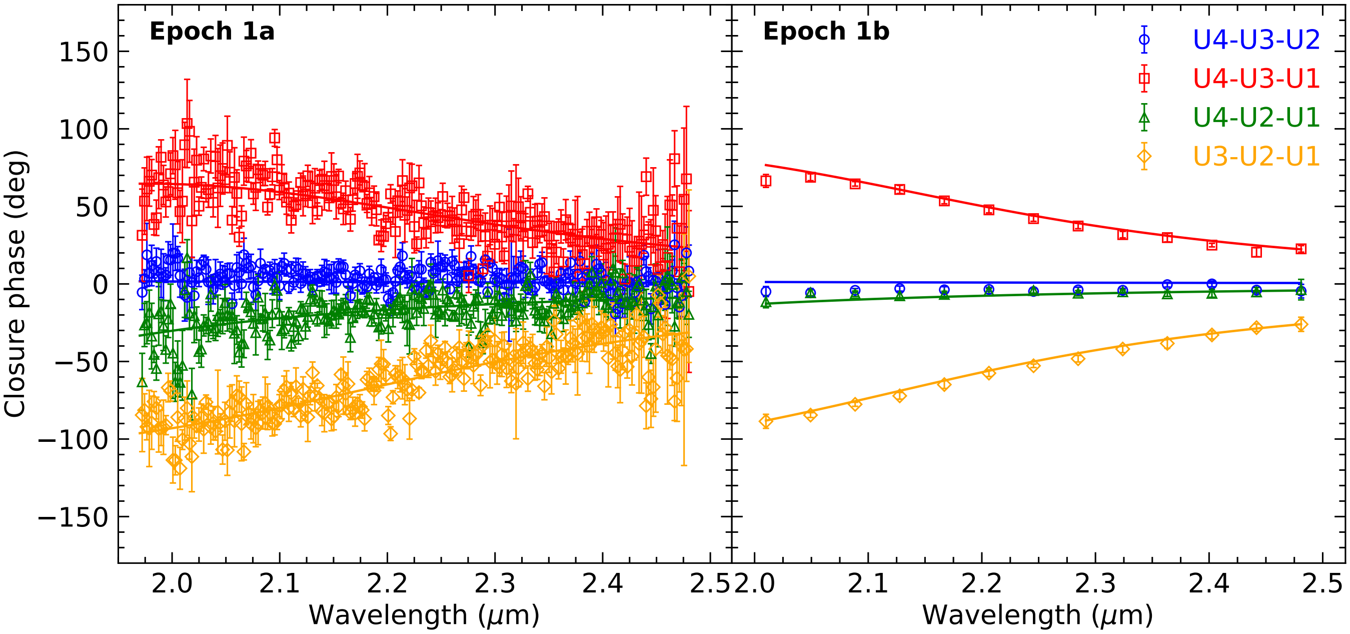

Figure 5. Closure-phase data for the VLTI epoch 1. The colored solid lines mark the best-fit microlensing model without the lens light.

east) PA = $\arctan \Delta\alpha/\Delta\delta$, the source–lens separation u (in Einstein radius units), and the angular Einstein radius $\theta_{\rm E}$. The latter quantity is calculated using the formula

$$\theta_{\rm E} = \frac{s\eta^{1/4}}{\sqrt{\eta}+1} \tag{8}$$

derived under the assumption that the flux ratio between the microlensed images determines their separation in Einstein radius units. Similarly, the source–lens separation is

$$u = \frac{1-\sqrt{\eta}}{\eta^{1/4}}. \tag{9}$$

The results of the fits to the individual epoch 2 exposures are presented in Table 6.

There is some tension between the medium- and low-resolution interferograms obtained during epoch 1: the measured $\Delta\alpha$ position differs by 3.3σ, the $\Delta\delta$ position by 2.3σ, and the position angle by3.2σ. On the other hand, the inferred angular Einstein radii are formally consistent between the three different data sets, although the differences between individual measurements can amount up to 1.5σ–2.9σ. These tensions indicate that at least one of the analyzed data sets may suffer from unaccounted-for, low-level systematic errors. Another explanation involves possible correlated noise in the closure-phase data that was not taken into account in evaluating the likelihood function (see Kammerer et al. 2020). Thus, the error bars reported in Tables 5 and 6 may be underestimated.

Further checks are possible because the flux ratio η and position angle PA of the images can be independently measured using the light-curve data (Section 4). In particular, there are two possible light-curve models differing by the sign of u_0, which predict the position angles of the microlensed images as $(-164.8^\circ, 31.5^\circ)$ (positive u_0) or $(-156.6^\circ, 14.3^\circ)$ (negative u_0), during the VLTI epochs 1 and 2, respectively. The measured angles $(-162.9^\circ, 26.7^\circ)$ (Table 5) seem to favor the $u_0 > 0$ model.

However, while the light-curve and closure-phase models agree well for epoch 1, the expected position angles differ by almost 4.8° (that is, 7.5σ) during epoch 2. That is illustrated in Figure 7, which presents 1σ, 2σ, and 3σ confidence ellipses in the (PA, η) plane. The gray contours mark the constraints from three different VLTI data sets, whereas the black contours are calculated based on the light-curve model ($u_0 > 0$). The blue, red, green, and orange contours mark the constraints on (PA, η) from OGLE, KMTC, KMTA, and KMTS data, respectively.

The position angle of the images measured from interferometric observations can be projected onto the $(\pi_{{\rm E},N}, \pi_{{\rm E},E})$ plane (Figure 4). The dotted and dashed lines in this figure correspond to the best-fitting values of the PAs during epochs 1a and 2, respectively. The dashed line does not intersect color contours from the light-curve model, which further exemplifies the tension discussed above.

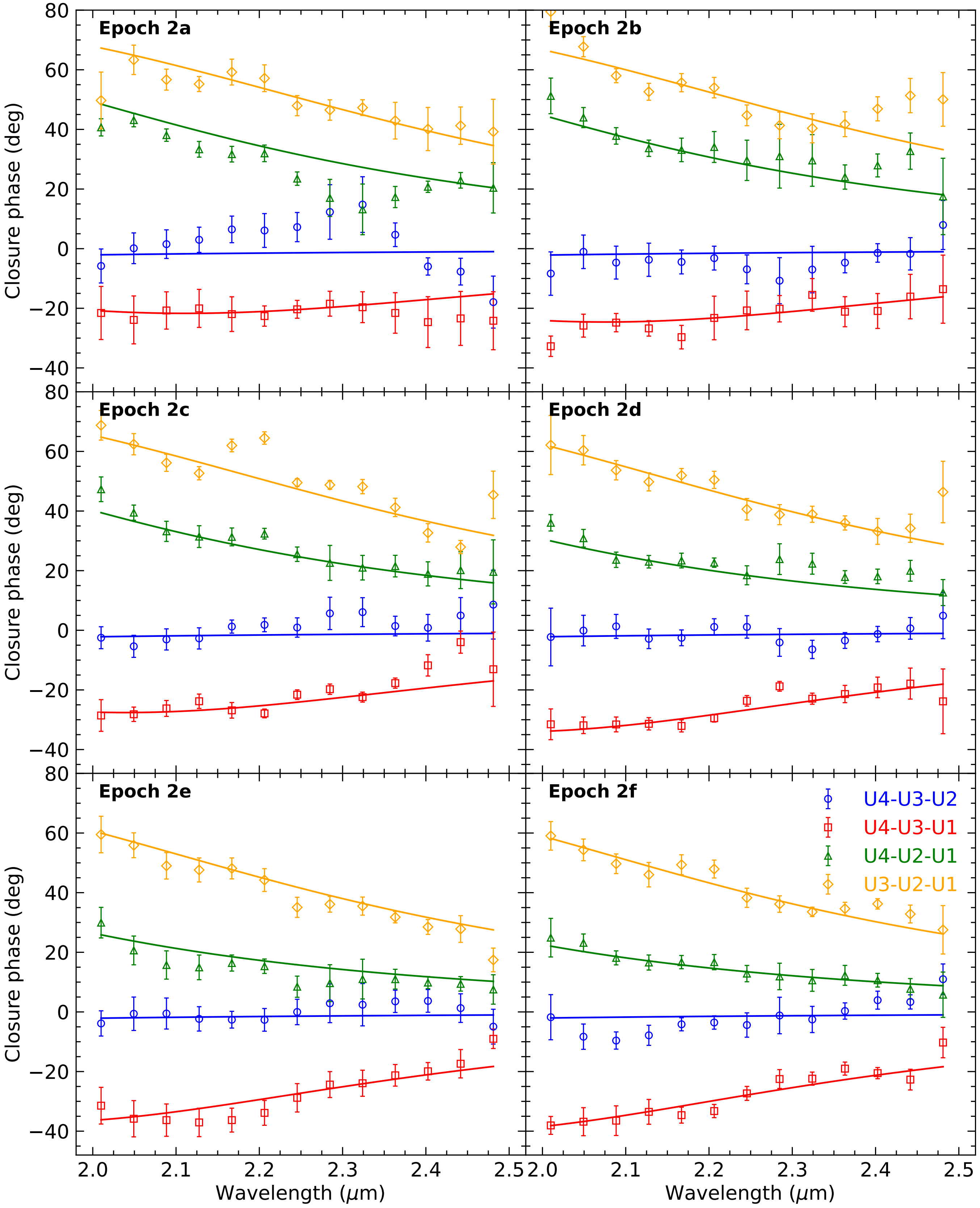

Figure 6. Closure-phase data for the VLTI epoch 2. The colored solid lines mark the best-fit microlensing model without the lens light.

The light-curve model also predicts the flux ratios between the microlensed images: $\eta = 0.5907 \pm 0009$ for epoch 1 and $\eta = 0.4264 \pm 0.0013$ for epoch 2. The former value is in 2.7σ–3.5σ tension with the closure-phase fits to epoch 1a and 1b data, respectively.

5.2. *Luminous Lens Model*

Despite the slight tensions discussed above, the simple binary star model overall describes the closure-phase data well (Figures 5 and 6). We now modify the model to include the possibility of blended light coming from the lens itself or a luminous companion (either to the lens or source). We change the primary parameters of the model to the lens–source separation u, the position angle of the lens relative to the source PA (which is equal to the position angle of the minor image relative to the major image), and the angular Einstein radius $\theta_{\rm E}$, which provide a more natural description of a microlensing event than the binary star model parameters. We keep σ_0 fixed at 6.990, 2.593, and 2.509 deg for epochs 1a, 1b, and 2, respectively.

We first consider models with a luminous lens. We place the lens in the origin of the coordinate system and calculate the positions of the minor and major image relative to it (Dong et al. 2019). We parameterize the ratio of the lens flux to the (unmagnified) source flux as $\eta_{\rm b}$.

We find that the closure-phase data do not provide strong evidence for the light from the lens. Including the lens light in the fits improves the χ^2 by 1.3, 0.1, and 0.9 for epochs 1a, 1b, and 2, respectively. The corresponding 95% upper limits on $\eta_{\rm b}$ are 0.74, 0.81, and 0.44, respectively. Moreover, we notice that the lens flux is correlated with the projected lens–source separation (and so the flux ratio between the microlensed images) and the angular Einstein radius.

Thus, we explore the possibility that the light from the lens may be a source of the tensions between the photometric and interferometric data discussed above. We repeat the modeling, taking into account the priors on u from the light-curve model. The best-fit parameters are reported in Table 7. While the tension between u determined from the light-curve model and that from the closure-phase model is removed, the position angles are still slightly different.

5.3. *Luminous Blend Model*

We also consider the model with a luminous blend, which has two additional parameters compared to the luminous lens model, the offset of the blend $(\Delta\alpha_{\rm b}, \Delta\delta_{\rm b})$ relative to the lens in the sky. We searched for possible blends on a grid of 201×201 positions uniformly spread over the range $-20 \leq \Delta\alpha_{\rm b}, \Delta\delta_{\rm b} \leq 20$ mas. We kept the position of the blend fixed but allowed the other parameters (u, PA, $\theta_{\rm E}$, and $\eta_{\rm b}$) to vary. The best-fit parameters were found using a downhill approach using the Nelder–Nead algorithm. We adopted a prior on the lens–source separation u from the light-curve model, and we required $\eta_{\rm b} \geq 0$.

The grid search results for the epoch 2 data are presented in Figure 8. There is only one local minimum around $(\Delta\alpha_{\rm b}, \Delta\delta_{\rm b}) = (-6.0, 15.8)$ mas that may be statistically significant (the χ^2 statistics is improved by $\Delta\chi^2 = 26.6$). We explored this local minimum using the MCMC approach and found $u = 0.4295 \pm 0.0016$, PA $= 26.00 \pm 0.24$ deg, $\theta_{\rm E} = 1.2672 \pm 0.0054$ mas, $\Delta\alpha_{\rm b} = -5.91 \pm 0.18$ mas, $\Delta\delta_{\rm b} = 15.73 \pm 0.32$ mas, and $\eta_{\rm b} = 0.0426 \pm 0.0094$. Thus, even if we consider this solution statistically significant, the blend does not explain the tension between the position angle measured using the light-curve and interferometric data.

5.4. *Final Closure-phase Models*

Finally, we measure the angular Einstein radius of the event $\theta_{\rm E}$ using all VLTI data combined. The baseline model has five parameters: the source–lens separations u and position angles of the images PA during epochs 1 and 2 and $\theta_{\rm E}$ (the same during both epochs). To estimate the impact of systematic errors on the parameter uncertainties, we employ the bootstrapping method (e.g., Efron 1979; Kervella et al. 2004; Lachaume et al. 2019). This involves randomly selecting eight VLTI interferograms (with replacement), feeding them to our fitting routine, and then repeating the procedure multiple times (in this case, 5000 times), to obtain the multivariate probability density function for the parameters of the model. Such a procedure enables us to retrieve more realistic uncertainties on the model parameters. The results of the bootstrapping method are reported in the second column of Table 8.

We then repeat the modeling, allowing an additional flux from the lens. We consider two models: with and without the prior on u from the light-curve model (the third and fourth columns of Table 8.) As in Section 5.2, we find that including the lens light does not significantly improve the fits, and we can only measure upper limits on $\eta_{\rm b}$ (95% confidence).

6. PHYSICAL PARAMETERS OF THE LENS

The mass and distance to the lens can be obtained from

$$M = \frac{\theta_{\rm E}}{\kappa \pi_{\rm E}}, \quad D_{\rm l} = \frac{\rm au}{\pi_{\rm E}\theta_{\rm E} + {\rm au}/D_{\rm s}}, \tag{10}$$

where $D_{\rm s} \approx 8$ kpc is the source distance. As the interferometric data do not provide strong evidence for the

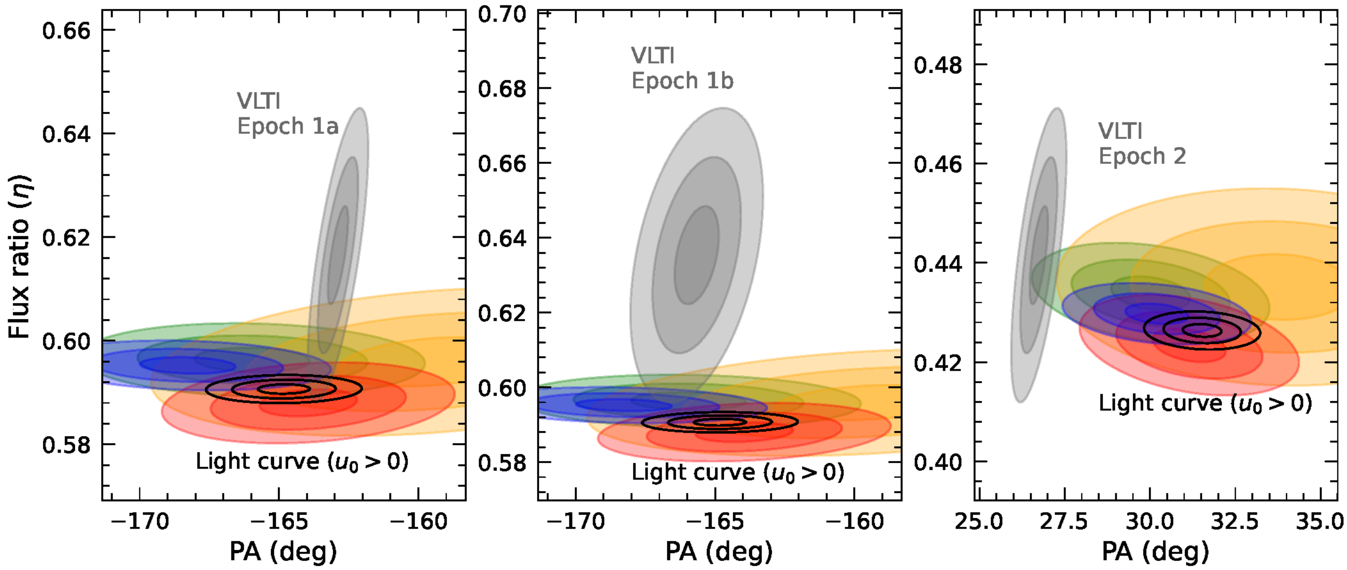

Figure 7. Constraints on the flux ratio and position angle of the microlensed images measured from the VLTI data (gray contours). The colored contours mark the constraints from the individual photometric data sets (blue—OGLE; red—KMTC; orange—KMTS; and green—KMTA), while the black contours are measured using all photometric data combined.

Table 6. Best-fit Parameters of the Closure-phase Model for Individual Epoch 2 Data Without the Lens Light

Parameter	Epoch 2a	Epoch 2b	Epoch 2c	Epoch 2d	Epoch 2e	Epoch 2f
$\Delta\alpha$ (mas)	1.114 ± 0.016	1.165 ± 0.017	1.200 ± 0.015	1.200 ± 0.012	1.115 ± 0.022	1.179 ± 0.018
$\Delta\delta$ (mas)	2.429 ± 0.085	2.374 ± 0.082	2.252 ± 0.054	2.283 ± 0.054	2.248 ± 0.045	2.335 ± 0.054
η	0.4010 ± 0.0238	0.4300 ± 0.0253	0.4698 ± 0.0253	0.4440 ± 0.0248	0.3649 ± 0.0306	0.4289 ± 0.0244
σ_0 (deg)	$1.35^{+0.95}_{-0.87}$	$2.23^{+1.07}_{-1.15}$	$3.53^{+0.65}_{-0.56}$	$1.34^{+0.58}_{-0.62}$	$0.56^{+0.59}_{-0.39}$	$1.71^{+0.65}_{-0.67}$
s (mas)	2.672 ± 0.079	2.644 ± 0.075	2.552 ± 0.047	2.579 ± 0.048	2.509 ± 0.035	2.615 ± 0.047
u	0.4608 ± 0.0295	0.4252 ± 0.0292	0.3800 ± 0.0283	0.4088 ± 0.0269	0.3649 ± 0.0306	0.4289 ± 0.0244
PA (deg)	24.64 ± 0.77	26.13 ± 0.80	28.04 ± 0.65	27.71 ± 0.60	26.36 ± 0.82	26.77 ± 0.70
$\theta_{\rm E}$ (mas)	1.3021 ± 0.0343	1.2933 ± 0.0328	1.2535 ± 0.0201	1.2633 ± 0.0199	1.2342 ± 0.0142	1.2790 ± 0.0193
χ^2/dof	51.6/48	50.6/48	47.5/48	40.2/48	28.6/48	46.5/48

Table 7. Best-fit Parameters of the Luminous Lens Closure-phase Model

Parameter	Epoch 1a	Epoch 1b	Epoch 2
u	0.2640 ± 0.0008	0.2640 ± 0.0008	0.4294 ± 0.0016
PA (deg)	-162.88 ± 0.36	-165.67 ± 0.72	26.77 ± 0.26
$\theta_{\rm E}$ (mas)	1.3266 ± 0.0114	1.3844 ± 0.0171	1.2868 ± 0.0066
$\eta_{\rm b}$	0.215 ± 0.078	0.370 ± 0.102	0.0662 ± 0.0394
η	0.5907 ± 0.0009	0.5907 ± 0.0009	0.4264 ± 0.0013
χ^2/dof	824.4/924	49.6/48	282.6/308

Table 8. Final Closure-phase Models

Parameter	No Blend	Luminous Lens	Luminous Lens (+ Prior on u)
$u(1)$	0.2317 ± 0.0125	0.2550 ± 0.0217	0.2634 ± 0.0002
PA(1) (deg)	-163.17 ± 1.00	-163.68 ± 1.29	-163.31 ± 0.81
$u(2)$	0.4286 ± 0.0122	0.4740 ± 0.0575	0.4306 ± 0.0004
PA(2) (deg)	26.40 ± 0.45	26.79 ± 0.51	26.60 ± 0.60
$\theta_{\rm E}$ (mas)	1.2802 ± 0.0085	1.3239 ± 0.0351	1.3082 ± 0.0110
$\eta_{\rm b}$	…	< 0.36	< 0.23

light from the lens, we adopt $\theta_{\rm E} = 1.2802 \pm 0.0085$ mas (Table 8) as our final measurement. Using $\pi_{\rm E} = 0.3330 \pm 0.0084$, we find $M = 0.472 \pm 0.012\,M_{\odot}$, $\pi_{\rm rel} =$

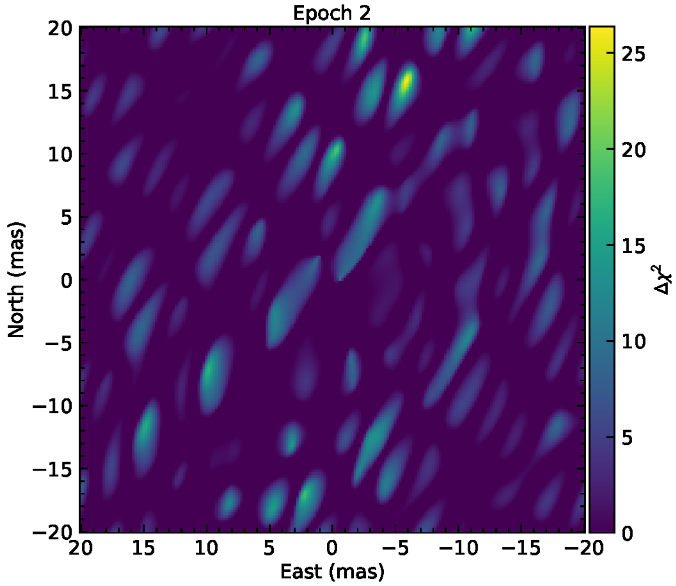

Figure 8. Detection map for possible luminous blends in the VLTI epoch 2 data. The color codes the χ^2 improvement over the model without the blend. The lens is located at the origin of the coordinate system.

0.426 ± 0.011 mas, and $D_\mathrm{l} = 1.81 \pm 0.05$ kpc. The lens is, therefore, most likely a main-sequence star located in the nearby Galactic disk. Alternatively, it may be a white dwarf. The mass function of field white dwarfs peaks at approximately $0.6\,M_\odot$ and falls steeply toward lower masses (e.g., Tremblay et al. 2016; Torres et al. 2021; Cunningham et al. 2024). Because white dwarfs less massive than $0.5\,M_\odot$ are much less frequent than main-sequence stars of that mass, we find this possibility unlikely.

If the lens is a main-sequence star, its absolute magnitude is $M_K = 5.76 \pm 0.04$ (Pecaut & Mamajek 2013), and its apparent K-band magnitude is 17.20 ± 0.07, assuming K-band extinction of 0.15 mag toward the lens (Nataf et al. 2013). That corresponds to $\eta_\mathrm{b} \approx 0.03$ in the K band, consistent with the limits on the lens flux from the VLTI data.

The trajectory of the source in the sky is presented in Figure 9 by a gray solid line. The open symbols (red square and blue circle) mark the positions of the source during the two epochs of VLTI observations, whereas the filled symbols mark the positions of the images of the source.

7. DISCUSSION AND CONCLUSIONS

The start of the scientific operations of GRAVITY Wide opens up completely new possibilities for the follow-up of microlensing events. Only very few of the brightest events could have been observed with the standard on-axis GRAVITY mode. In contrast, GRAVITY Wide observations provide the opportunity for studies of a large sample of events and measurements of masses, distances, and transverse velocities of isolated objects, including neutron stars and black holes. Interferometric observations are very efficient at the same time—only a 1 hr exposure is sufficient for determining the angular Einstein radius. That is in stark contrast to astrometric microlensing measurements, which require time-consuming monitoring lasting several years (Sahu et al. 2022; Lam et al. 2022). Astrometric measurements are also more susceptible to systematic errors due to blending than interferometric observations (Mróz et al. 2022). Thus, as argued by Gould (2023), interferometric observations with GRAVITY Wide (and its successor, GRAVITY+) hold promise for routine detections of isolated neutron stars and stellar remnants.

In this paper, we report the first successful observation of a microlensing event with GRAVITY Wide and the resolution of microlensed images in the event OGLE-2023-BLG-0061/KMT-2023-BLG-0496. These observations serve as a test bed for verifying the capabilities of the new instrument. In particular, some observations were carried out using the low-resolution mode, which

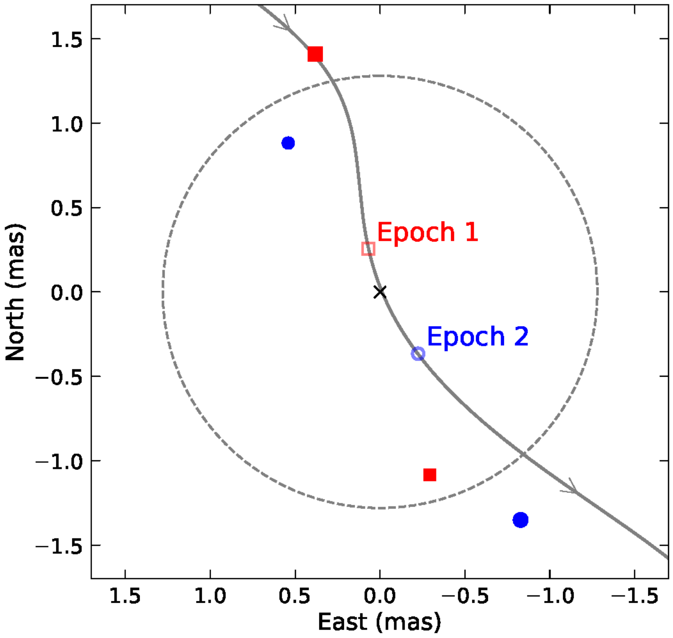

Figure 9. Geometry of the event. The gray solid line marks the trajectory of the source relative to the lens (black cross) in the sky. The open symbols (red square and blue circle) mark the positions of the source during the two epochs of VLTI observations. The filled symbols (red squares and blue circles) mark the positions of the two images of the source observed during epoch 1 and epoch 2, respectively. The dashed circle shows the Einstein radius.

had never been tried before with GRAVITY Wide. The comparison of medium- and low-resolution interferograms (epochs 1a and 1b) reveals low-level systematic differences between the inferred parameters of the lensing system (Table 5). Similar systematic differences can be seen in models fitted to individual exposures taken during epoch 2 (Table 6). Judging from Figures 5 and 6, the systematic and correlated errors in the closure phase data can reach up to 5–10 deg. We defer a detailed investigation of the systematic errors in the closure-phase data to a separate study.

We use the bootstrapping method to deal with these systematic and correlated errors. Thanks to the large number of observations, we are still able to measure the angular Einstein radius with a subpercent precision, $\theta_{\rm E} = 1.2802 \pm 0.0085\,{\rm mas}$. By combining the information from the light-curve and the closure-phase data, we measure the mass of the lens with a precision of 2.6%, $M = 0.472 \pm 0.012\,M_{\odot}$.

Independent tests of the accuracy of the closure-phase model are possible with the light-curve model. The model of the microlensing event light curve predicts the brightness ratio of the microlensed images and their position angle in the sky. While the predicted flux ratio matches that inferred from the closure-phase data reasonably well (Figure 7), there is a tension in the position angles measured using the epoch 2 data. This tension cannot be explained by additional blended light in the closure-phase data (Section 5.3).

One possible explanation for this systematic difference is the unaccounted-for systematic errors in the closure-phase data. Alternatively, the problem may lie in the light-curve model. However, we find this unlikely, because the residuals from the best-fit light-curve model are smaller than ≈ 0.01 mag, and there is no strong evidence that the light-curve model is inadequate. A binary-lens model can be ruled out, because the binary lens would produce additional images of the source, which should have been detected in our grid search. Still, the unaccounted-for orbital motion of the source (the "xallarap effect") could, in principle, partly explain the discrepancy. The xallarap effect would not create additional images but would deflect the path of the source on the sky. Our modeling, however, does not provide strong evidence for xallarap in the light-curve data (Appendix A).

The additional testing of the model presented in this paper will be possible thanks to the data from the *Gaia* satellite (Gaia Collaboration et al. 2016). OGLE-2023-BLG-0061/KMT-2023-BLG-0496 was observed and alerted by the *Gaia* Photometric Science Alerts system (Hodgkin et al. 2021) as Gaia23ckg. Time-series astrometric data collected by *Gaia*, when made public later this decade, may reveal deflection due to astrometric microlensing effects and enable independent measurements of the angular Einstein radius.

ACKNOWLEDGEMENTS

We thank David Bennett and Łukasz Wyrzykowski for their comments on the manuscript.

Based on observations collected at the European Southern Observatory under ESO program 108.220D. This research was funded in part by the National Science Centre, Poland, grants OPUS 2021/41/B/ST9/00252 and SONATA 2023/51/D/ST9/00187 awarded to P.M. This research is partly supported by the National Natural Science Foundation of China (grant No. 12133005) and the science research grants from the China Manned Space Project with No. CMS-CSST-2021-B12. S.D. acknowledges the New Cornerstone Science Foundation through the XPLORER PRIZE.

GRAVITY+ is developed by the Max Planck Institute for Extraterrestrial Physics, the Institute National des Sciences de l'Univers du CNRS (INSU), with its institutes LESIA / Paris Observatory-PSL, IPAG / Grenoble Observatory, Lagrange / Côte d'Azur Observatory, and CRAL / Lyon Observatory, the Max Planck Institute for Astronomy, the University of Cologne, the CENTRA—Centro de Astrofisica e Gravitação, the University of Southampton, the Katholieke Universiteit Leuven, and the European Southern Observatory. D.D. has received funding from the European Research Council (ERC) under the European Union's Horizon 2020 research and innovation program (grant agreement CoG—866070).

This research has made use of the KMTNet system operated by the Korea Astronomy and Space Science Institute (KASI) at the three host sites of CTIO in Chile, SAAO in South Africa, and SSO in Australia. Data transfer from the host site to KASI was supported by the Korea Research Environment Open NETwork (KREONET). This research was supported by KASI under the R&D program (project No. 2024-1-832-01) supervised by the Ministry of Science and ICT. W.Zang, H.Y., S.M., R.K., J.Z., and W.Zhu acknowledge support by the National Natural Science Foundation of China (grant No. 12133005). W.Zang acknowledges the support from the Harvard–Smithsonian Center for Astrophysics through the CfA Fellowship. J.C.Y. and I.-G.S. acknowledge support from U.S. NSF grant No. AST-2108414. Y.S. acknowledges support from BSF grant No. 2020740. The work by C.H. was supported by grants from the National Research Foundation of Korea (2019R1A2C2085965 and 2020R1A4A2002885). J.C.Y.

acknowledges support from a Scholarly Studies grant from the Smithsonian Institution.

REFERENCES

Albrow, M. D., Horne, K., Bramich, D. M., et al. 2009, MNRAS, 397, 2099

Arsenault, R., Alonso, J., Bonnet, H., et al. 2003, in Society of Photo-Optical Instrumentation Engineers (SPIE) Conference Series, Vol. 4839, Adaptive Optical System Technologies II, ed. P. L. Wizinowich & D. Bonaccini, 174–185

Bachelet, E., Zieliński, P., Gromadzki, M., et al. 2022, A&A, 657, A17

Cassan, A., Ranc, C., Absil, O., et al. 2022, Nature Astronomy, 6, 121

Colavita, M. M., Wallace, J. K., Hines, B. E., et al. 1999, ApJ, 510, 505

Cunningham, T., Tremblay, P.-E., & W. O'Brien, M. 2024, MNRAS, 527, 3602

Dalal, N., & Lane, B. F. 2003, ApJ, 589, 199

Delplancke, F. 2008, NewAR, 52, 199

Delplancke, F., Górski, K. M., & Richichi, A. 2001, A&A, 375, 701

Dong, S., Mérand, A., Delplancke-Ströbele, F., et al. 2019, ApJ, 871, 70

Efron, B. 1979, The Annals of Statistics, 7, 1

Einstein, A. 1936, Science, 84, 506

Eisenhauer, F., Monnier, J. D., & Pfuhl, O. 2023, ARA&A, 61, 237

Foreman-Mackey, D., Hogg, D. W., Lang, D., & Goodman, J. 2013, PASP, 125, 306

Gaia Collaboration, Prusti, T., de Bruijne, J. H. J., et al. 2016, A&A, 595, A1

Gaia Collaboration, Vallenari, A., Brown, A. G. A., et al. 2023, A&A, 674, A1

Gould, A. 1994, ApJL, 421, L71

Gould, A. 2004, ApJ, 606, 319

Gould, A. 2023, arXiv e-prints, arXiv:2310.19164

Gould, A., Miralda-Escude, J., & Bahcall, J. N. 1994, ApJL, 423, L105

GRAVITY Collaboration, Abuter, R., Accardo, M., et al. 2017, A&A, 602, A94

GRAVITY+ Collaboration, Abuter, R., Allouche, F., et al. 2022, A&A, 665, A75

Hodgkin, S. T., Wyrzykowski, L., Blagorodnova, N., & Koposov, S. 2013, Philosophical Transactions of the Royal Society of London Series A, 371, 20120239

Hodgkin, S. T., Harrison, D. L., Breedt, E., et al. 2021, A&A, 652, A76

Hog, E., Novikov, I. D., & Polnarev, A. G. 1995, A&A, 294, 287

Kammerer, J., Mérand, A., Ireland, M. J., & Lacour, S. 2020, A&A, 644, A110

Kendrew, S., Hippler, S., Brandner, W., et al. 2012, in Society of Photo-Optical Instrumentation Engineers (SPIE) Conference Series, Vol. 8446, Ground-based and Airborne Instrumentation for Astronomy IV, ed. I. S. McLean, S. K. Ramsay, & H. Takami, 84467W

Kervella, P., Ségransan, D., & Coudé du Foresto, V. 2004, A&A, 425, 1161

Kim, H.-W., Hwang, K.-H., Shvartzvald, Y., et al. 2018, arXiv e-prints, arXiv:1806.07545

Kim, S.-L., Lee, C.-U., Park, B.-G., et al. 2016, J. Korean Astron. Soc., 49, 37

Lachaume, R., Rabus, M., Jordán, A., et al. 2019, MNRAS, 484, 2656

Lacour, S., Dembet, R., Abuter, R., et al. 2019, A&A, 624, A99

Lam, C., Lu, J. R., Udalski, A., et al. 2022, ApJL, 933, L23

Lam, C. Y., & Lu, J. R. 2023, ApJ, 955, 116

Lawrence, A., Warren, S. J., Almaini, O., et al. 2007, MNRAS, 379, 1599

Lucas, P. W., Hoare, M. G., Longmore, A., et al. 2008, MNRAS, 391, 136

Mérand, A. 2022, in Society of Photo-Optical Instrumentation Engineers (SPIE) Conference Series, Vol. 12183, Optical and Infrared Interferometry and Imaging VIII, ed. A. Mérand, S. Sallum, & J. Sanchez-Bermudez, 121831N

Minniti, D., Lucas, P. W., Emerson, J. P., et al. 2010, NewA, 15, 433

Miyamoto, M., & Yoshii, Y. 1995, AJ, 110, 1427

Mróz, P., Udalski, A., & Gould, A. 2022, ApJL, 937, L24

Nataf, D. M., Gould, A., Fouqué, P., et al. 2013, ApJ, 769, 88

Nemiroff, R. J., & Wickramasinghe, W. A. D. T. 1994, ApJL, 424, L21

Pecaut, M. J., & Mamajek, E. E. 2013, ApJS, 208, 9

Poleski, R., & Yee, J. C. 2019, Astronomy and Computing, 26, 35

Rybicki, K. A., Wyrzykowski, Ł., Bachelet, E., et al. 2022, A&A, 657, A18

Sahu, K. C., Anderson, J., Casertano, S., et al. 2022, ApJ, 933, 83

Shao, M., & Colavita, M. M. 1992, A&A, 262, 353

Shappee, B. J., Prieto, J. L., Grupe, D., et al. 2014, ApJ, 788, 48

Skowron, J., Udalski, A., Gould, A., et al. 2011, ApJ, 738, 87

Skrutskie, M. F., Cutri, R. M., Stiening, R., et al. 2006, AJ, 131, 1163

Smith, M. C., Mao, S., & Paczyński, B. 2003, MNRAS, 339, 925

Torres, S., Rebassa-Mansergas, A., Camisassa, M. E., & Raddi, R. 2021, MNRAS, 502, 1753

Tremblay, P. E., Cummings, J., Kalirai, J. S., et al. 2016, MNRAS, 461, 2100

Udalski, A. 2003, AcA, 53, 291

Udalski, A., Szymański, M. K., & Szymański, G. 2015, AcA, 65, 1

Walker, M. A. 1995, ApJ, 453, 37

Witt, H. J., & Mao, S. 1994, ApJ, 430, 505

Woillez, J., Wizinowich, P., Akeson, R., et al. 2014, ApJ, 783, 104

Woźniak, P. R. 2000, AcA, 50, 421

Wu, Z., Dong, S., Mérand, A., et al. 2024a, ApJ, 977, 229

Wu, Z., Dong, S., Yi, T., et al. 2024b, AJ, 168, 62

Yang, H., Yee, J. C., Hwang, K.-H., et al. 2024, MNRAS, 528, 11

Zang, W., Dong, S., Gould, A., et al. 2020, ApJ, 897, 180

APPENDIX

A. XALLARAP MODELS

In this section, we explore whether the orbital motion of the source (xallarap effect) can explain the discrepancy between the position angle of the microlensed images measured using VLTI data and calculated from the light-curve model. Compared to the standard point-source point-lens model, models including the xallarap effect have seven additional parameters describing the shape of the source's orbit. These are P_ξ – the orbital period; a_ξ – the semimajor axis (expressed in Einstein radius units); i_ξ – the inclination of the orbit; Ω_ξ – the longitude of the ascending node of the orbit; u_ξ – the argument of latitude at the reference epoch (which is taken to be $t_{0,\xi} = t_{0,\mathrm{par}}$); e_ξ – the eccentricity of the orbit; and ω_ξ – the argument of periapsis of the orbit.

For simplicity, we consider only circular orbits, keeping $e_\xi = 0$ and $\omega_\xi = 0$. We also assume that the companion to the source is dark, given there is no strong evidence for the additional light in the VLTI data (Section 5.3). We employ the MulensModel package by Poleski & Yee (2019) to calculate the source trajectory and magnification.

We search for best-fit xallarap models on a grid of orbital periods P_ξ spanning from 10 to 251 days. We keep the orbital period fixed, but the remaining parameters (a_ξ, i_ξ, Ω_ξ, u_ξ, and the standard microlensing parameters) are allowed to vary. The best-fit parameters are found using the MCMC approach (Foreman-Mackey et al. 2013). Simultaneously, we calculate the position angle of the minor image relative to the major image during the two epochs of VLTI observations (Section 4). We assume uniform priors on all parameters.

The results of our calculations for the OGLE data are presented in Table 9, where we report the χ^2 statistic of the best-fit model and the predicted position angles. There is no strong evidence for xallarap in the data. The best-fit model, for the orbital period of $P_\xi = 79.4$ days, is favored over the model without xallarap by only $\Delta\chi^2 = 11.6$, which is not statistically significant given the increased number of free parameters. The predicted position angles are all similar to those calculated using the standard point-source point-lens model. However, their uncertainties are typically larger, which quantifies the additional degrees of freedom on the position of the source due to orbital motion.

Table 9. Results of Xallarap Fits to the OGLE Data

P (days)	χ^2	PA(1) (deg)	PA(2) (deg)
No xallarap	542.9	-168.37 ± 1.83	30.12 ± 0.99
10.0	539.6	-168.75 ± 1.57	29.07 ± 5.48
12.6	540.5	-168.69 ± 1.30	27.25 ± 5.47
15.8	538.5	-168.73 ± 1.63	29.37 ± 5.42
20.0	538.6	-168.51 ± 1.37	28.89 ± 5.36
25.1	540.3	-168.11 ± 1.45	29.69 ± 5.50
31.6	541.3	-168.24 ± 1.42	29.26 ± 5.20
39.8	534.0	-168.79 ± 2.46	29.07 ± 5.22
50.1	532.9	-169.33 ± 2.87	29.68 ± 4.59
63.1	534.0	-169.34 ± 3.86	29.39 ± 5.87
79.4	531.3	-169.42 ± 2.80	29.90 ± 5.43
100	531.5	-169.85 ± 10.16	29.40 ± 5.17
126	537.2	-169.39 ± 29.20	29.12 ± 5.49
158	541.1	-168.72 ± 6.08	29.29 ± 5.32
200	540.2	-168.40 ± 29.12	29.76 ± 5.17
251	540.7	-168.44 ± 3.96	29.40 ± 5.46